



The elevated temperature oxidation and wear behavior of Fe₂₀Co₂₀Ni₂₀Cr₈Mo₁₂B₁₀Si₁₀ high-entropy alloy coating by laser cladding

Guosong Zhang ^{a,*}, Zongjia Zhang ^a, Jiyuan Xuan ^a, Bing Chen ^a, Di Jiang ^{a,**}, Xiaojie Song ^b

^a School of Mechanical and Electronic Engineering, Shandong University of Science and Technology, Qingdao, 266590, China

^b School of Materials Science and Engineering, Shandong University of Science and Technology, Qingdao, 266590, China



ARTICLE INFO

Keywords:

Laser cladding
Fe₂₀Co₂₀Ni₂₀Cr₈Mo₁₂B₁₀Si₁₀
Microstructure
Wear resistance
Oxidation resistance

ABSTRACT

High-entropy alloy coatings show great potentiality in improving elevated temperature oxidation and wear resistance. In this study, Fe₂₀Co₂₀Ni₂₀Cr₈Mo₁₂B₁₀Si₁₀ high-entropy alloy coating was prepared on 42CrMo alloy structural steel by laser cladding. The elevated temperature oxidation and wear resistance were investigated at room temperature and elevated temperature (600 °C). The crystal structure of the coating changed from a dual-phase structure consisting of BCC (dominant phase) and FCC phase to a single FCC structure with the production of SiO₂, MoO₃, Cr₂O₃ and NiCr₂O₄ after 600 °C oxidation for 200 h. The oxidation rate of the coating was 1.21 × 10⁻³ mg/(mm²·h), one fifth that of 42CrMo steel. The tribological properties of the coating shown no significant difference at room and elevated temperature with an average coefficient of friction and the wear rate about 0.46 and 0.02 mm³/N·m, respectively. The oxide film generated on the surface of the coating was dense and uniform, providing excellent oxidation and wear resistance at elevated temperature.

1. Introduction

A stable and effective braking device is one of the important devices to ensure train safety during high-speed operation. In the braking process, the brake disc will be subjected to thermal wear of about 600 °C instantly, and the oxidized brake disc material will lead to the decline of material wear resistance [1,2]. Therefore, surface strengthening technology has become a research hot spot to improve the elevated temperature wear resistance of the brake disc and enhance its service life. Studies have shown, compared to improving the overall performance of the material, that coatings prepared on the material surface can not only improve the wear and elevated temperature oxidation resistance, but also save costs [3,4].

It is noteworthy that the tribological properties of mechanical components are not only affected by the hardness, but also have a great relationship with the modulus of elasticity, fracture toughness and the components [5]. Nanoindentation is a suitable technique to evaluate the mechanical properties of mechanical components, which provides some information about the hardness (H), the elastic modulus (E), the plasticity index (H/E), the yield pressure (i.e., resistance to plastic deformation, H^3/E^2) as well as the elastic recovery (η) [6]. Among them, the

plasticity index is widely recognized as an important index for determining the limit of elastic behavior in surface contact, and it is essential for the study of the wear resistance of materials. The elastic recovery is the ratio between the elastic deformation energy and the total deformation energy, which can indicate how much energy is released from the material after loading, and is particularly important in applications involving impact loading [7].

Laser cladding with a low dilution rate, fast cooling rate, small thermal deformation [8,9], and metallurgical bonding between the coating and the substrate [10–12] displays huge advantage in improving the surface properties of metal workpiece with small deformation [13, 14]. The performance of materials depend on the material composition and preparation process. High entropy alloys have received considerable attention since they were proposed in 2004 [15–17]. The research results show that the laser cladding high entropy alloy coating with high hardness, high thermal stability, high corrosion resistance and high wear resistance can be prepared by selecting a reasonable element ratio and preparation process [18–21].

Owing to the small difference in the mixing enthalpy and atomic size of Fe, Co, Ni and Cr elements, FeCoNiCr series high entropy alloys are easy to form a uniform single solid solution and show excellent

* Corresponding author.

** Corresponding author.

E-mail addresses: zhguosong@sdu.edu.cn (G. Zhang), jiangdi1210@163.com (D. Jiang).

performance, so the effect of the composition and laser cladding process parameters on their performances was studied by many researchers [22–26]. The laser-cladded FeNiCoCrMo HEA coating presents higher hardness at low laser power due to the Mo-enriched phases precipitating at grain boundaries, because Mo-enriched phases cannot fully diffuse with the main phase at a low laser power [27]. It has been found that the addition of Mo elements promotes the formation of hard σ phases of FeCoNiCrMo_x HEA coating, and the microhardness increased with increasing Mo content [28]. The excellent wear resistance of the laser-cladded FeCrNiCoB_x HEA coatings can give the credit to the formation of (Cr, Fe)₂B hard phases and significantly refined grains [29]. The addition of Si elements leads to the lattice distortion and promotes the formation of Si-enriched intermetallic compounds, which significantly improve the hardness and wear resistance of the FeCoCrNiMoSi_x coating [30]. Moreover, the addition of Si elements can improve the elevated temperature oxidation resistance due to the formation of SiO₂ layer on the surface [31,32].

For FeCoNiCr based alloy coating, the addition of Mo element can improve the wear resistance of the coating and the ratio of Cr element to Mo element is reduced appropriately to improve the mechanical properties of the coating [33]. In addition, the doping of B and Si elements is beneficial for the formation of coatings, and enhance the deoxygenation and slag removal ability, wear resistance and oxidation resistance of coatings at the same time [34]. In this study, Fe₂₀Co₂₀Ni₂₀Cr₈Mo₁₂B₁₀Si₁₀ HEAs was designed by theoretical calculation suitable for brake disc cladding, and prepared using laser cladding. Since the brake disc material was subjected to high temperature impacts during braking, the elevated temperature oxidation resistance of HEA coating and substrate was studied and the effect of high temperature (600 °C) on the phase, microstructure and wear resistance of HEA coatings and substrates were analyzed. Considering the sustainability of brake disk materials in practical applications, the tribological properties of coatings and substrates before and after elevated temperature oxidation at different temperatures were also analyzed, which was significant for the further application of HEA coatings in brake disc materials for high-speed trains.

2. Materials and methods

2.1. Raw materials

42CrMo steel, a material for brake discs, was selected as the substrate material in this study. The specimens (150 × 100 × 50 mm) were grinded with a grinder to remove the surface oxide skin, and smoothed with 240 # sandpaper. Before cladding, the specimens were washed with deionized water after ultrasonic clean out for 30 min in anhydrous ethanol, and treated by 60 °C in a constant temperature drying oven for 2 h, then baked. The metal powder was made of Fe, Co, Cr, Ni, Mo, Si, and boron iron powder with a particle size of 50–100 μ m, and were weighed according to the mass ratio of different elements as shown in Table 1. The mass fractions of elements in boron iron powder are: 20% B, 4.0% Si, 0.5% C, 0.2% P, 0.5% Al, and the remaining Fe. Subsequently, a vertical planetary ball mill (DECO-PBM-V-2L) was used to mix the raw material powder with a 400 r/min mill speed and 10:1 ball material ratio for 4 h. The mixed power was dried for 2 h at 150 °C for backup.

2.2. Laser cladding process

In this study, the fiber semiconductor laser (LSJG-BGQ-2000) was used for multi-channel preset powder laser cladding with a spot

diameter of 3 mm as shown in Fig. 1 [35]. The powder featured a preset thickness of 1 mm. During the laser cladding process, argon gas was introduced for protection with a flow rate of 25 L/min. The process parameters of laser cladding included a scanning speed of 600 mm/min, a laser power of 1800 W, a spot diameter of 3 mm and an overlap rate of 50%. The prepared coatings and 42CrMo were processed into specimens with sizes of 10 × 10 × 15 mm through wire cutting and fixed into shape by inlay technique. The specimens were polished after sanding with 60 #, 240 #, 500 #, 1000 # and 2000 # sandpaper due to the presence of oxide layer and unmelted metal powder on the surface of the coating after laser cladding. The thickness of the treated coating was approximately 0.5 mm. Then, the prepared specimens were used to test the physical phase, microstructure, microhardness, elevated temperature oxidation and abrasion resistance.

2.3. Characterization methods

X-ray diffraction (XRD) was used to analyze phase of the prepared high entropy alloy coating using Cu-K α target as the radiation source with a working voltage of 40 kV, working current of 40 mA, a diffraction angle range of 20°–100°, and the scanning speed of 4°/min. The polished specimen was etched with aqua regia (HCl:HNO₃ = 3:1).

Scanning electron microscope (SEM) of Nova NanoSEM 450 type (FEI, USA) was used to observe the microstructure of the surface and cross section of the specimens before and after elevated temperature oxidation with an acceleration voltage of 20 KV and a beam spot size of 3.0 mm–4.0 mm. The JEOL JXA-8230 electron probe (EPMA) was used to observe and analyze the morphology of the wear on the surface of the specimens. The equipped X-ray energy spectrometer (EDS) was used to analyze the types and contents of micro elements in the material. TMVS-1 micro Vickers hardness tester was used to test the Vickers hardness of the specimens with a load of 1.96 N and a loading time of 15 s.

KSL-1200X muffle furnace was used to conduct elevated temperature oxidation experiments of the specimens with a temperature of 600 °C and a total oxidation time of 200 h. The specimens were placed in an Al₂O₃ crucible due to possibility of oxide shedding from the surface of the specimens during the oxidation process at elevated temperature. The specimens were weighed together with the crucible in order to avoid the influence of the shedding oxides on the experimental results. Three sets of identical specimens were prepared to reduce experimental errors, and elevated temperature oxidation weight gain data were calculated and averaged. For the convenience of description in subsequent figures, elevated temperature oxidation for 100 and 200 h are referred to as EO-100 and EO-200, respectively, before elevated temperature oxidation is referred to as BO.

Multi-functional friction and wear testing machine (MFT-5000, RTEC USA) was used to conduct reciprocating sliding wear tests with a diameter of 5 mm on specimens before and after elevated temperature oxidation at room temperature. A rotating ball disc configuration was used to test the wear of the specimens before and after elevated

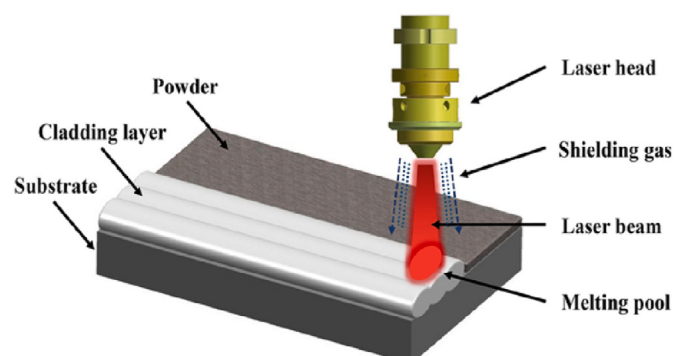


Fig. 1. Schematic diagram of laser cladding.

Table 1

Chemical composition of the coating (wt%).

Fe	Co	Ni	Cr	Mo	FeB	Si
13.02	21.72	21.64	7.67	21.22	9.95	4.78

temperature oxidation at 600 °C, and the radius of friction wear was 2.5 mm.

According to actual working conditions, each test was carried out with a load of 30 N, a linear speed of 10 mm/s and a duration of 30 min. Si_3N_4 ceramic ball with a diameter of 10 mm was used as grinding ball and the friction coefficient time relationship curve was obtained after the experiment. Three sets of identical specimens were prepared to demonstrate the reproducibility and accuracy of the experiments, and the final experimental data obtained were not significantly different. A three-dimensional profilometer (Micro XAM) was used to measure the wear volume. The morphology and composition analysis of the worn surface were observed by SEM and EDS.

3. Results and discussion

3.1. Elevated temperature oxidation behavior

3.1.1. Macroscopic morphology

The oxide surface macroscopic morphology of the specimens after elevated temperature oxidation for 100 and 200 h are shown in Fig. 2. Elevated temperature oxidation for 100 h, amounts of oxides exhibited on 42CrMo steel material surface due to the poor antioxidant properties. However, the surface of the coating underwent minimal changes with only slight oxidation observed. When the elevated temperature oxidation time increased to 200 h, severe peeling of oxide skin on 42CrMo steel surface had occurred, and the surface continued to oxidize internally with repeatedly generating oxides after peeling. For the coating, a dense and uniform oxide formed on the surface accompanied by slight oxide skin peeling, which indicated that the coating had excellent elevated temperature oxidation resistance.

3.1.2. Phase analysis

The XRD patterns of the surfaces of the specimens before and after elevated temperature oxidation are shown in Fig. 3. The crystal structure of 42CrMo steel presented a single-phase BCC before elevated temperature oxidation. There was no significant difference in the physical phase composition of 42CrMo steel after elevated temperature oxidation for 100 and 200 h, which consisted of Fe_2O_3 and Fe_3O_4 . After sanding 0.25 mm (half of the coating thickness referred to as C-0.25) off the surface of the specimen oxidized for 200 h, it was found that Fe_2O_3 still existed, which indicated that oxygen had diffused into the interior of 42CrMo steel specimen. However, Fe_3O_4 was not observed in the C-0.25 specimen due to the degree of oxidation inside the 42CrMo steel was less

than that on the surface.

The crystal structure of the coating presented BCC (dominant phases) and FCC with FeSi_2 precipitate before the elevated temperature oxidation. Elevated temperature oxidation for 100 h, most of BCC phase transformed into FCC phase which became the dominant structure of the coating, and the oxidation product containing SiO_2 , MoO_3 and Cr_2O_3 appeared on the coating surface with the decomposition and oxidation of FeSi_2 at elevated temperature [36,37]. When the elevated temperature oxidation time increased to 200 h, the surface layer of the coating presented a single-phase FCC structure with a new NiCr_2O_4 phase. The diffraction peak intensity of BCC decreased at a distance of 0.25 mm from the coating surface which explained that a proportion of BCC phase transformed into FCC phase during elevated temperature oxidation process. Moreover, the peak of oxides were not found, indicating that the coating had excellent elevated temperature oxidation resistance due to the compact and homogeneous NiCr_2O_4 oxide film on the surface hindering further diffusion of oxygen elements [38].

3.1.3. Microstructure and EDS analysis

Surface morphologies and energy spectrum of the specimens after elevated temperature oxidation are shown in Figs. 4–7. Elevated temperature oxidation for 100 h, a thick oxide layer with severe cracks generated on the surface of 42CrMo steel as shown in Fig. 4(a). For the coating, as shown in Fig. 4(c), the surface generated inhomogeneous oxides due to compositional segregation caused by laser cladding. The region with more oxidation products was enriched with elements Mo, B and O confirmed by EDS mapping (Fig. 5) and point analysis listed in Table 2. The reason why this area was more prone to oxidation was due to the enrichment of Mo elements easy to generate MoO_3 [39]. The region located point C, was enriched with elements Fe, Co, Ni and Si, and formed fewer oxidation products. Si elements could improve the elevated temperature oxidation resistance of high entropy alloys by acting as an activator of Cr, increasing the activity of Cr in the alloy and making it easier to form protective oxide Cr_2O_3 [40]. Dense Cr_2O_3 and SiO_2 oxide layer hindered the reaction of deeper layers of the coating with oxygen elements and reduced the oxide production rate.

When the elevated temperature oxidation time increased to 200 h, there was no stripping due to the formation of a dense oxide film on the surface of the coating. Compared to elevated temperature oxidation for 100 h, the area with more oxidation products had become a region rich in Fe, Co, Ni and Si elements, as shown in Fig. 6 and Table 3. The volatilization of MoO_3 at elevated temperature resulted to the reducing of oxidation products on the area rich in Mo and B elements. For the

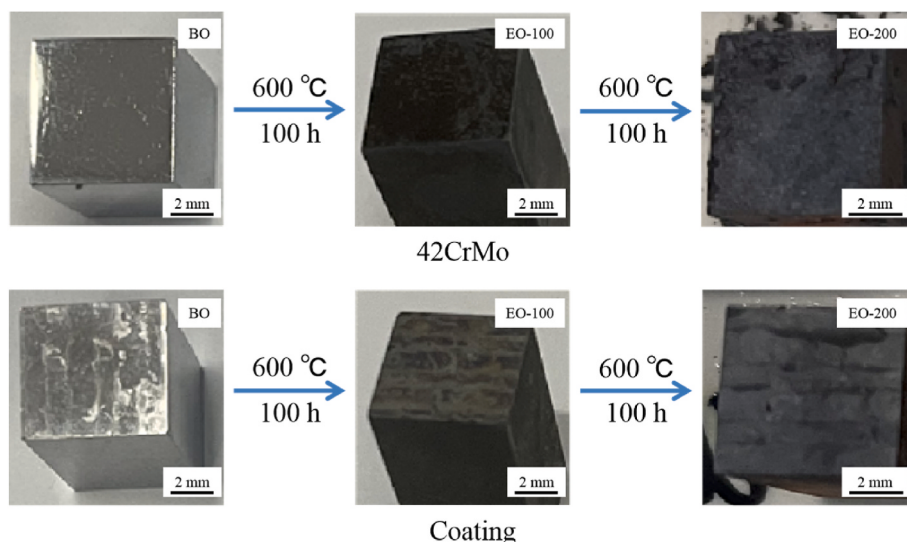


Fig. 2. The oxide surface macroscopic morphology of 42CrMo steel and coating.

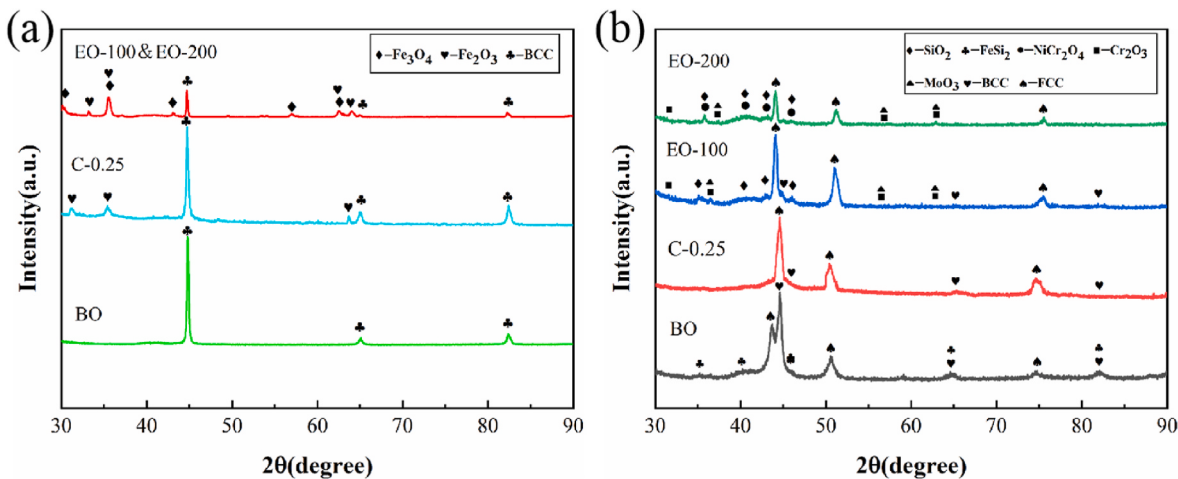


Fig. 3. XRD patterns of 42CrMo steel and coating: (a) 42CrMo; (b) Coating.

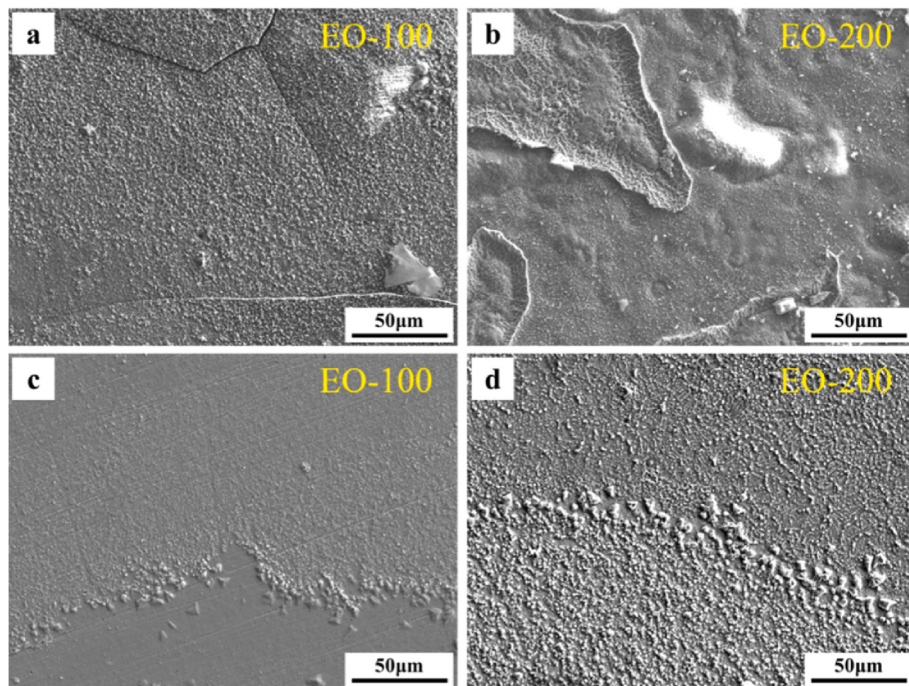


Fig. 4. Surface morphology of 42CrMo steel and coating: (a–b) 42CrMo; (c–d) Coating.

region rich in Fe, Co, Ni and Si elements, the oxidation products with a new NiCr₂O₄ produced which had excellent adhesion and antioxidant properties continued to increase as the oxidation time increased. Moreover, the presence of SiO₂ could increase the contact area between the oxide layer and the coating, thereby increasing the bonding strength between the oxide layer and the coating, effectively preventing the oxide layer from falling off [41]. For the 42CrMo steel, the oxides generated on the surface of 42CrMo steel exhibited generous peeling as shown in Fig. 4(b). After peeling, the new oxides generated by re-oxidation of the surface, then continued to peel. The oxides generated on the surface were analyzed with XRD and EDS (Fig. 7 and Table 4) to be Fe₂O₃ and Fe₃O₄, respectively, where Table 4 showed the chemical compositions within the red boxed area in Fig. 7.

SEM images and EDS of the specimens before and after elevated temperature oxidation are shown in Figs. 8–11. It was found that the uniform flaky pearlitic structure was distributed on the surface and in the cross-section of 42CrMo steel before oxidation with a uniform

distribution of Fe elements (Fig. 8). The surface of 42CrMo steel after elevated temperature oxidation was covered with O elements and the microstructure was transformed into the granular pearlite structure (Fig. 9), which led to the decrease of surface properties. Fig. 9(b) showed the cross-sectional microstructure of 42CrMo steel at about 0.25 mm from the surface, it could be seen that the O elements was also distributed in this region due to the severe oxidation of the 42CrMo steel. However, the cross-section had lower levels of oxidation compared to the surface, which could be observed from the fact that some flaky pearlitic structure was still present within the cross-section.

For the coating, it was found that the coating featured dense and homogeneous structures, and the coating transitioned from surface to depth as equiaxed crystals to dendritic crystals to columnar crystals. Fe, Co, Ni and Si elements were enriched in the dendrite region formed FCC phase, while Mo and B elements were enriched in the interdendritic region formed BCC phase as analyzed by EDS (Fig. 10). Elevated temperature oxidation for 200 h (Fig. 11), the dendrite region increased and

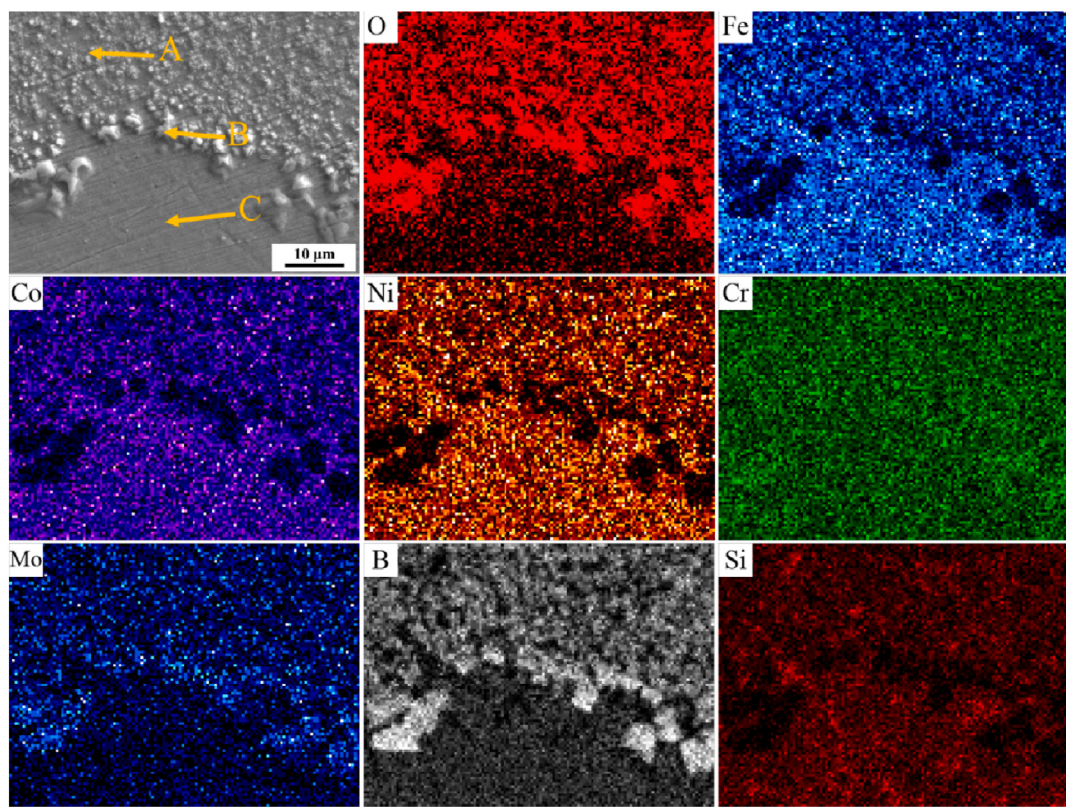


Fig. 5. Surface morphology and EDS analysis of the coating after elevated temperature oxidation for 100 h.

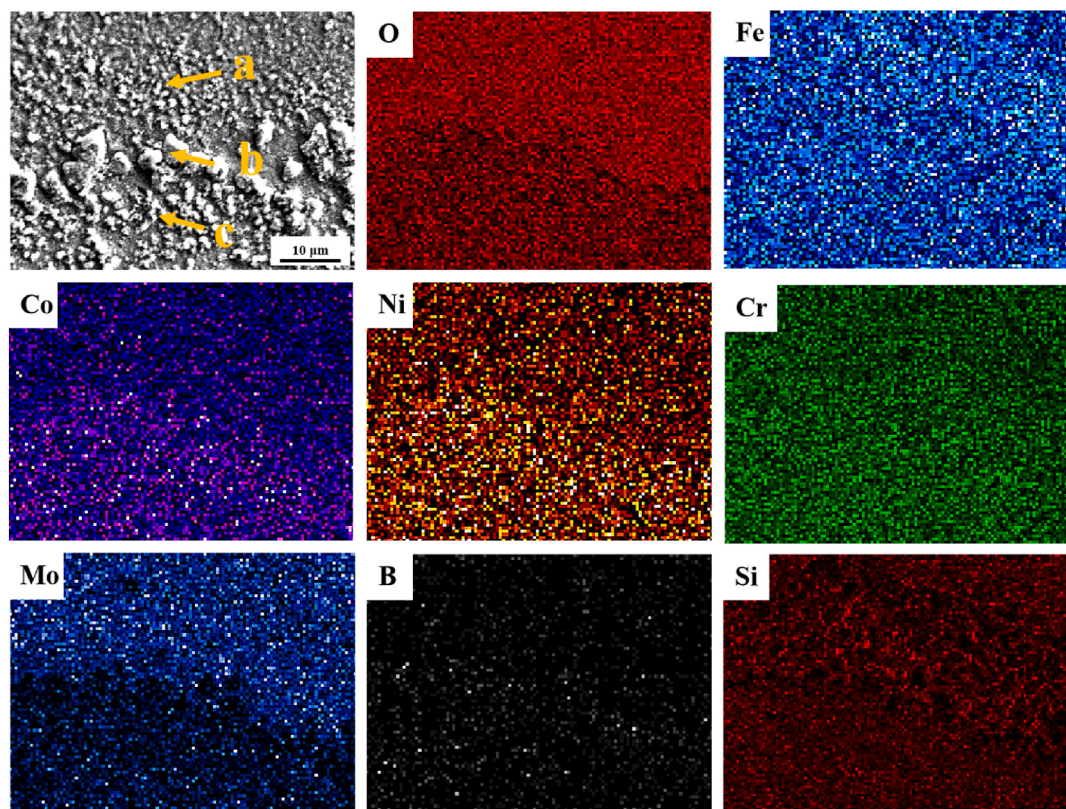


Fig. 6. Surface morphology and EDS analysis of the coating after elevated temperature oxidation for 200 h.

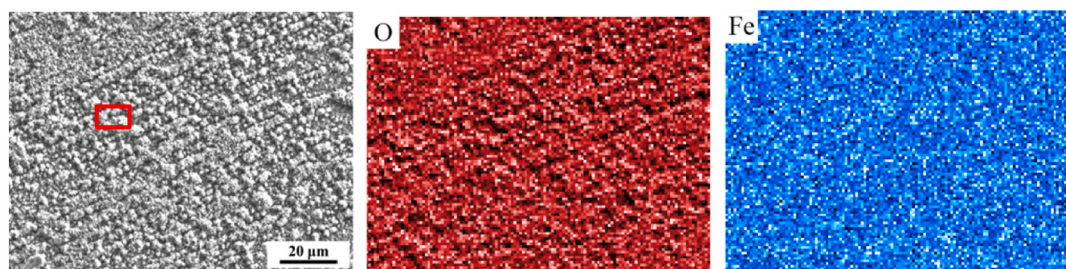


Fig. 7. Surface morphology and EDS analysis of 42CrMo steel after elevated temperature oxidation for 200 h.

Table 2

Chemical composition of different regions marked in Fig. 5.

Element	Fe	Co	Ni	Cr	Mo	B	Si	O
A	13.97	9.03	7.60	7.42	31.44	8.72	1.43	20.38
B	7.68	3.67	2.16	7.21	43.18	8.34	0.24	27.62
C	16.99	12.66	13.88	9.89	13.09	8.11	11.71	13.67

Table 3

Chemical composition of different regions marked in Fig. 6.

Element	Fe	Co	Ni	Cr	Mo	B	Si	O
a	13.53	12.20	10.44	9.02	17.55	4.72	3.20	29.34
b	15.78	13.92	9.30	14.84	7.27	4.36	4.11	30.42
c	8.89	11.61	11.57	19.12	9.25	4.05	5.73	29.78

Table 4

Chemical composition of the region marked in Fig. 7.

Element	Fe	O	C
Composition	61.78	36.79	1.43

the interdendritic region decreased, which was consistent with the decrease of BCC phase and the increase of FCC phase in the XRD results. Furthermore, the O elements was observed on the surface and top of the cross-section of the coating, which indicates that the top of the coating was oxidized. However, the O elements was not observed in the middle (about 0.25 mm from the surface) and bottom of the cross-section of the coating, which meant that the interior of the coating was not oxidized.

3.1.4. Mechanical property analysis

The average microhardness and microhardness curves of the specimens surface before and after elevated temperature oxidation are shown in Fig. 12. Before oxidation, the microhardness of the coating was 659.9 HV_{0.2}, which was about 3.5 times that of 42CrMo steel. The microhardness decreased to 609.6 HV_{0.2} after elevated temperature oxidation for 200 h due to the transformation from BCC phase to FCC phase. In addition, the hard FeSi₂ phase was susceptible to oxidation and decomposition at elevated temperature resulting in the formation of softer oxides, which also led to the reduction of the microhardness. However, the decrease of microhardness was not significant due to the

generation of brittle oxides on the surface. After a long period of elevated temperature oxidation, the internal structure of the coating grew further and became more dense. At the same time, the oxide film generated on the surface could effectively prevent oxidation inside the coating and the BCC phase was still partially present in the interior of the coating. Therefore, the microhardness of the C-0.25 coating decreased from that before oxidation, but it was higher than that of the oxidized coating, which was about 619.5 HV_{0.2}. The microhardness of 42CrMo steel increased from 179.7 HV_{0.2} to 254.7 HV_{0.2} due to the generation of friable oxide layer. The C-0.25 substrate decreased to 158.9 HV_{0.2} owing to the oxidation and softening of the internal structure after elevated temperature oxidation. Furthermore, the microhardness of the coating at 600 °C was lower compared to after elevated temperature oxidation due to the softer oxides at elevated temperature, which was about 549.7 HV_{0.2}. Similarly, the microhardness of 42CrMo steel at 600 °C was lower compared to after oxidation at elevated temperature, which was about 201.6 HV_{0.2}.

As shown in Fig. 12(b), the hardness curves of coatings exhibited a cliff-like shape, declining from the coating zone (CZ) to heat-affected zone (HAZ) to the substrate zone (SZ). The microhardness of the top of the coating cross-section after elevated temperature oxidation was lower than that before oxidation, which was consistent with the results of the average microhardness of the surface. The cross-section microhardness of the coatings tended to be consistent as the depth was increased to about 0.3 mm. For the 42CrMo steel, the microhardness decreased with the increase of the cross-section depth and became

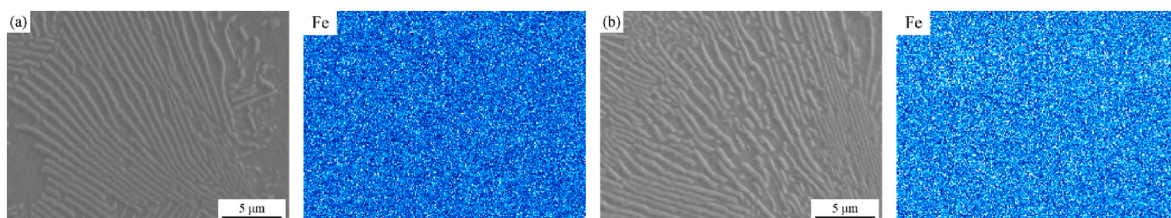


Fig. 8. SEM images and EDS of 42CrMo steel before oxidation: (a) Surface; (b) Cross-section.

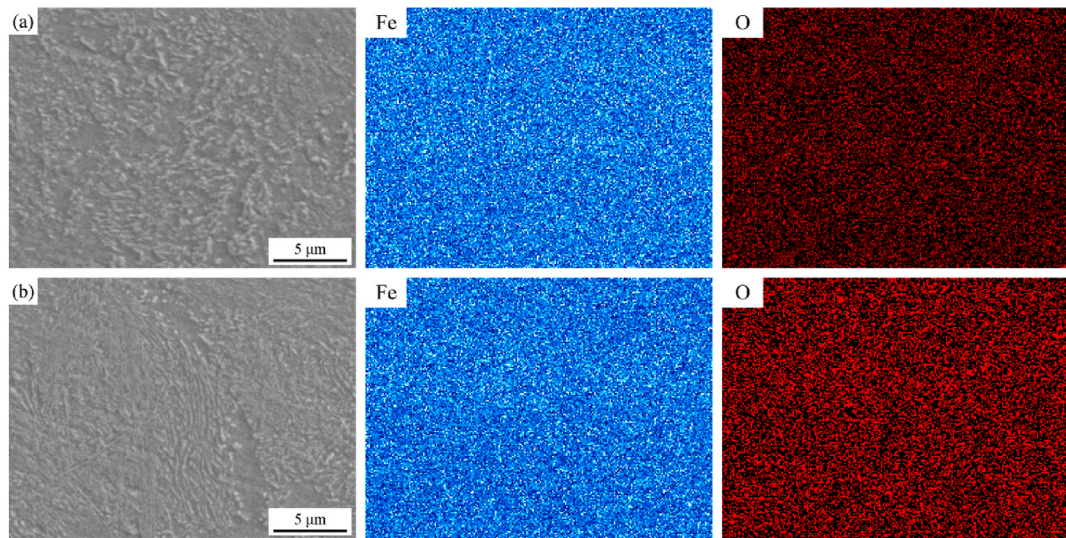


Fig. 9. SEM images and EDS of 42CrMo steel after oxidation: (a) Surface; (b) Cross-section.

progressively lower than the microhardness of surface before oxidation. The microhardness of 42CrMo steel gradually increased when the depth of the cross-section was increased to about 0.35 mm.

In order to analyze the correlation between elevated temperature-induced phase transition and the wear behavior of the coating, the nanoindentation test was conducted and the results were shown in Fig. 13. For convenience of description, the BCC phase and FCC phase before and after elevated-temperature oxidation were referred to as BO-BCC, BO-FCC, and EO-200-FCC, respectively. Apparently, the maximum indentation depth of the BO-BCC phase was lower than that of the BO-FCC phase and EO-200-FCC phase, exhibiting the highest nanohardness of 10.79 GPa. The EO-200-FCC phase exhibited the lowest nanohardness and highest elastic modulus due to the growth of grains and diffusion of elements caused by elevated temperature, which were 7.89 GPa and 353.75 GPa, respectively. In addition, the EO-200-FCC phase had the lowest H/E and H^3/E^2 values, indicating a poor resistance to plastic deformation. And the values of H/E and H^3/E^2 were positively correlated with wear resistance. Therefore, the decrease in mechanical properties caused by the phase transition at elevated temperature also led to a decrease in the wear resistance of the coating [7].

3.1.5. Oxidation kinetics analysis

The oxidation kinetics curve of the specimens are shown in Fig. 14. The oxidation weight gain can be calculated by the following formula:

$$\delta_i = W_{i+1} - W_i \quad (1)$$

where, $\delta_{i(i=1,2,3 \dots, 10)}$ is the oxidation weight gain of i-th of the specimen of 42CrMo steel, $W_{i(i=1,2,3 \dots, 10)}$ is the mass of the i-th weighing of the specimen of 42CrMo steel.

$$\delta_j = W_{j+1} - W_j - \delta_j \times \frac{S_1 - S_2}{S_1} \quad (2)$$

where, $\delta_{j(j=1,2,3 \dots, 10)}$ is the oxidation weight gain of j-th of the coating, $W_{j(j=1,2,3 \dots, 10)}$ is the mass of the j-th weighing of the coating, S_1 is the total surface area of the specimen, and S_2 is the surface area of the coating.

$$\delta'_i = \delta_i \times S_2 \quad (3)$$

where, $\delta'_i(i=1,2,3 \dots, 10)$ is the oxidation weight gain of i-th of 42CrMo steel with the same surface area as the coating.

As shown in the figure, the weight gain of 42CrMo steel increased rapidly as prolonging the testing time due to the poor antioxidant

properties, but the weight gain of the coating increased very slowly. Oxidation index and oxidation rate are important parameters to characterize the high temperature oxidation process. The empirical formula Wanger oxidation is often used in the kinetics of metal oxidation at elevated temperatures, as follows:

$$\left(\frac{\delta}{S}\right)^2 = k_p t \quad (4)$$

where, δ is the oxidation weight gain, S is the surface area of the specimens, k_p is a constant representing oxidation rate, and t is the oxidation time. By calculation, the oxidation rates of 42CrMo steel and coating at each stage were shown in Table 5. The average oxidation rates of 42CrMo steel and coating were 6.1×10^{-3} mg/(mm²·h) and 0.87×10^{-3} mg/(mm²·h), respectively. It was obvious that the coating had a lower oxidation rate, indicating that the coating had more excellent antioxidant properties [42].

3.2. Room temperature tribological performance

3.2.1. Coefficient of friction

The coefficient of friction(COF) curves and the average COF of the specimens before and after elevated temperature oxidation at room temperature are shown in Fig. 15. In the primary stage, the COF rose sharply due to severe plastic deformation caused by the extrusion of abrasive balls into the coating surface. The COF of the specimens surface existed a certain difference in the early stage of wear due to the oxide film formed after elevated temperature oxidation which could be used as a lubricant to resist a certain amount of wear [43]. As the wear test progressed, the COF stabilized due to the periodic accumulation and elimination of wear debris.

Compared with 42CrMo steel, the COF of the coating (about 0.47) before and after elevated temperature oxidation was smaller due to the higher microhardness and more stable in the later stages of wear, which met the COF requirements (about 0.4) of brake discs for high-speed trains. The average COF of 42CrMo steel after elevated temperature oxidation decreased from 0.61 to 0.57 due to the increase in microhardness after elevated temperature oxidation. The average COF of the coating before and after elevated temperature oxidation was not significantly discrepancy due to the excellent elevated temperature oxidation resistance and abrasion resistance of the SiO₂ and NiCr₂O₄ oxide films formed on the surface of the coating after elevated temperature oxidation, which effectively prevented further oxidation of the coating.

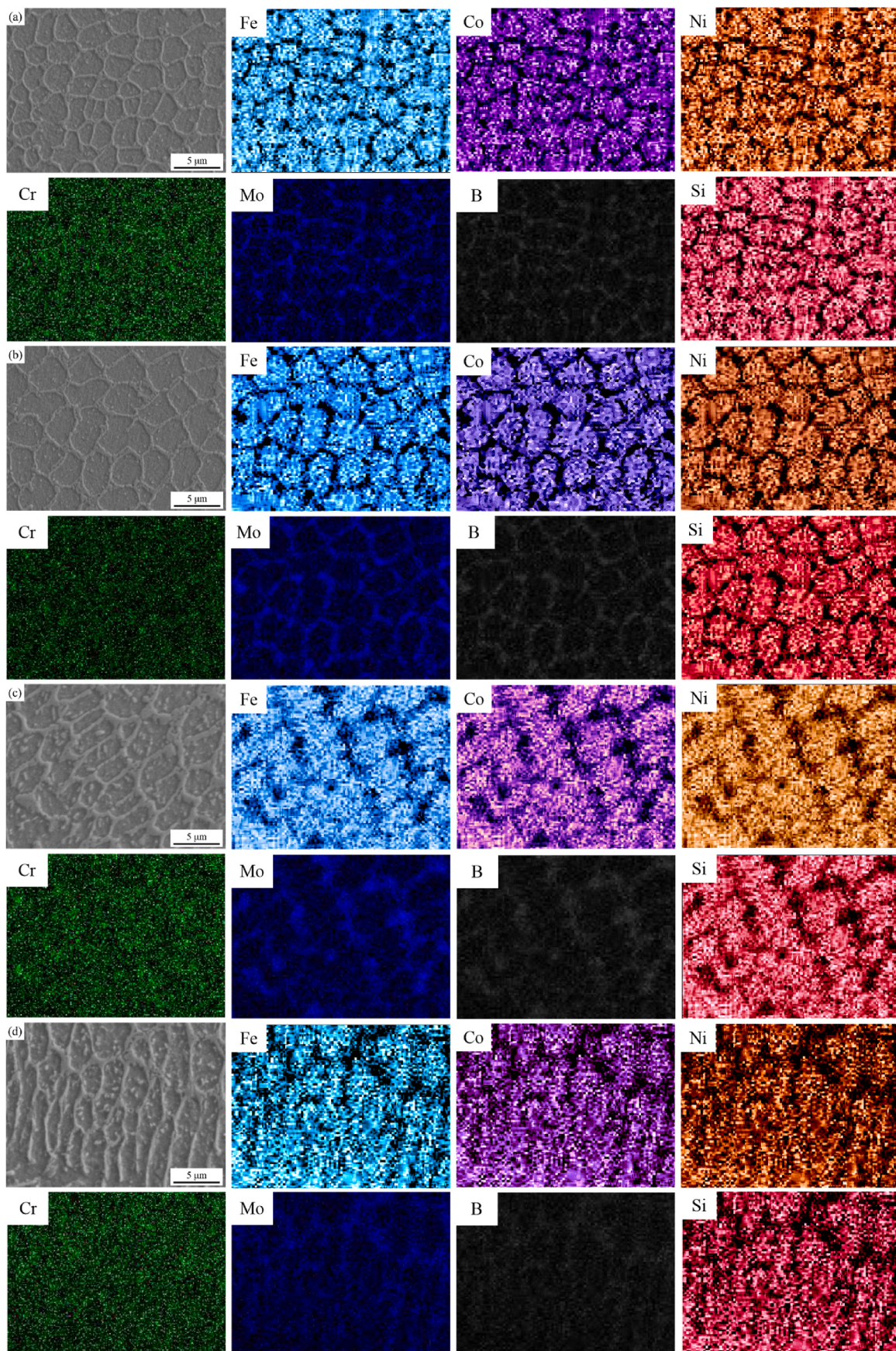


Fig. 10. SEM images and EDS of the coating before oxidation:
(a) Surface; (b) Top of cross-section; (c) Middle of cross-section; (d) Bottom of cross-section.

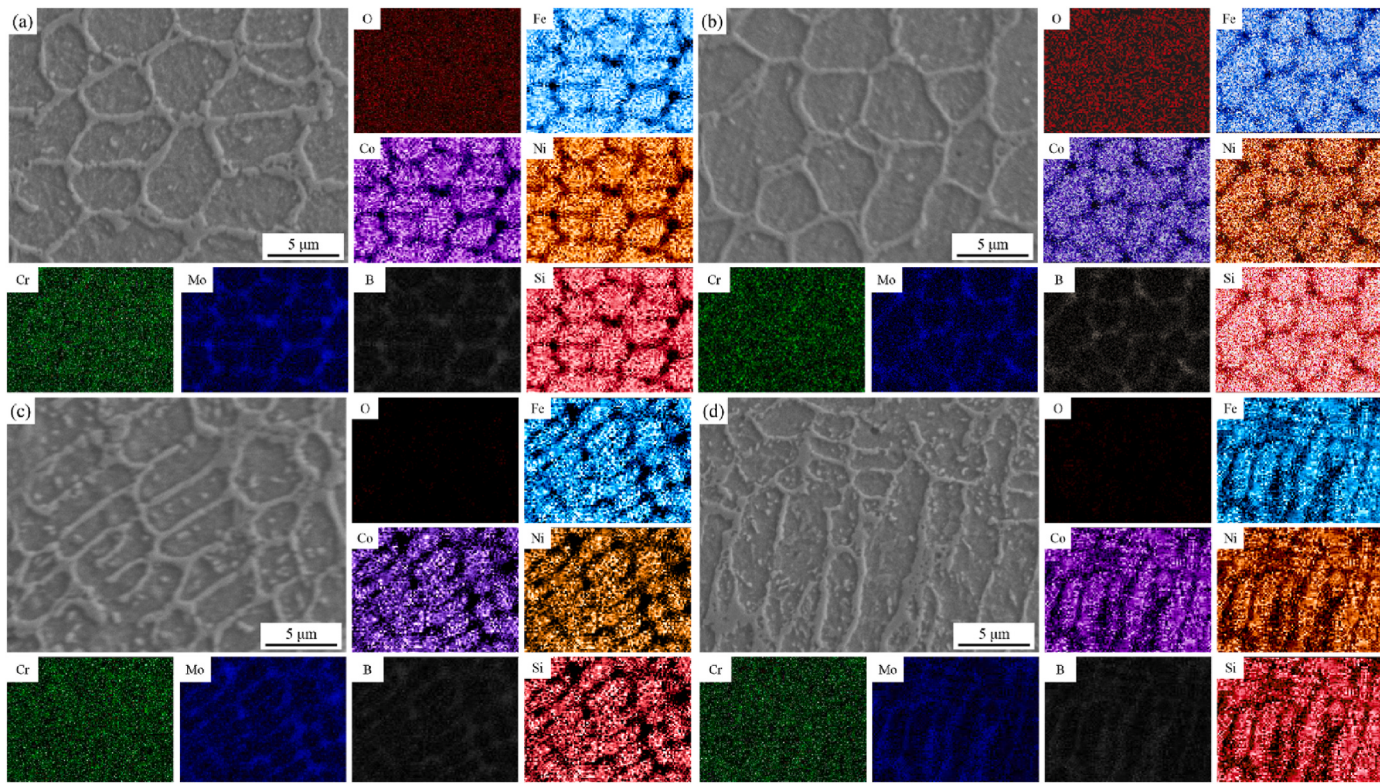


Fig. 11. SEM images and EDS of the coating after oxidation:
(a) Surface; (b) Top of cross-section; (c) Middle of cross-section; (d) Bottom of cross-section.

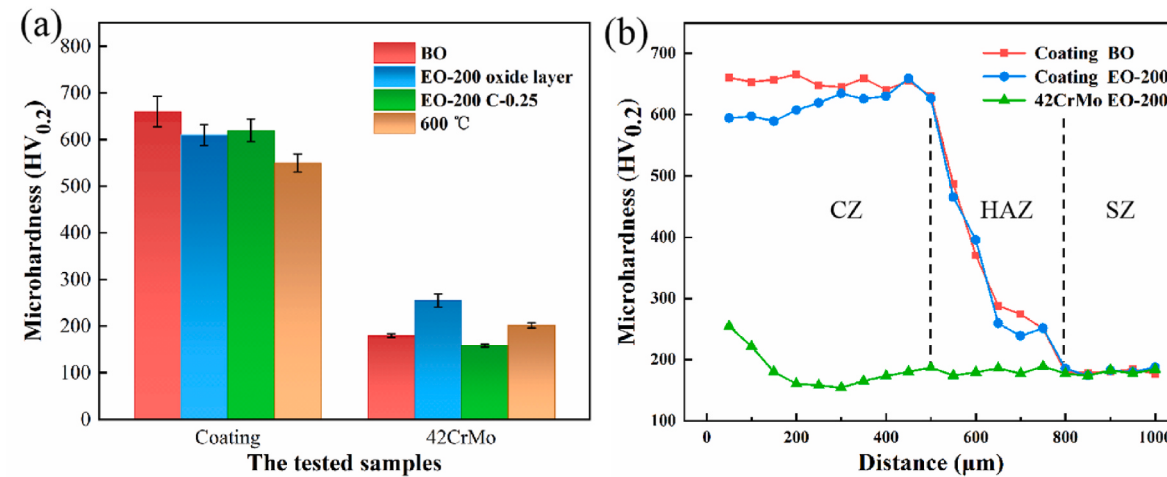


Fig. 12. Microhardness of 42CrMo steel and coating: (a) Average microhardness; (b) Microhardness curves.

3.2.2. Wear morphology

To investigate the effect of oxidation on the wear behavior of the specimens at room temperature, SEM analysis was conducted on the wear surface, and the results are shown in Figs. 16 and 17. The wear surface before elevated temperature oxidation of the coating was relatively flat with shallow wear marks and no hard phase peeling. Oxidative wear was additionally observed owing to the appearance of a partially oxidized layer, which was due to the reduction of the oxidation activation energy of metal elements by friction heat, leading to friction oxidation reactions. Grooves were wide and deep after elevated temperature oxidation and the formation of grooves and chips illustrated the mechanism of abrasive wear [44]. The wear resistance of the coating was reduced due to the decrease in microhardness after elevated

temperature oxidation. In addition, the lower H/E and H^3/E^2 values result in a poor resistance to plastic deformation of the coating surface, which led to deeper grooves on the surface of the coating. Besides, oxidative wear was additionally observed owing to the appearance of a protective oxide layer [45].

Compared with the coating, a significant number of grooves exhibited on the surface of 42CrMo steel due to the peeling of the hard phase, resulting in three body abrasive wear between 42CrMo steel, stripped particles, and friction balls. According to SEM analysis, the O and Si elements distributed on the wear surface of 42CrMo steel before elevated temperature oxidation, indicating that 42CrMo steel surface had been oxidized and plastic deformation occurred between 42CrMo steel and the friction ball, resulting in adhesive wear. This revealed that

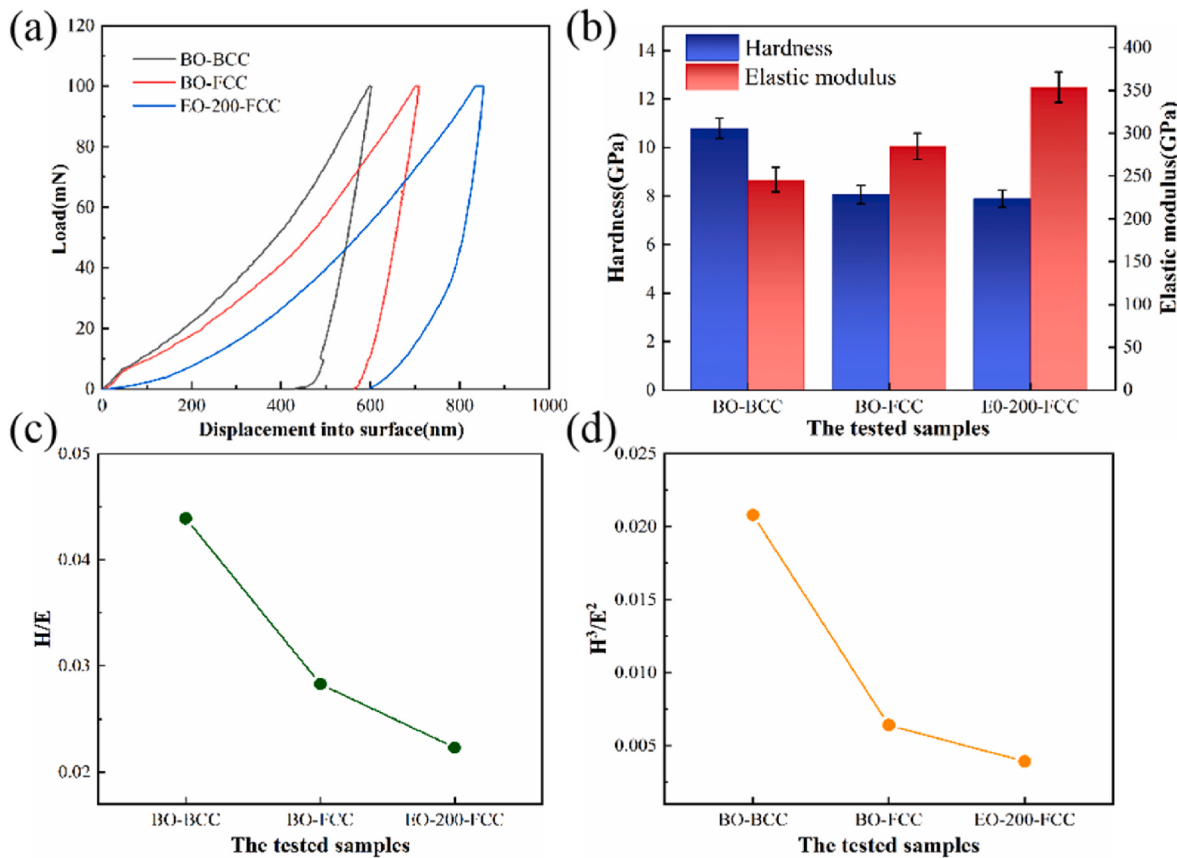


Fig. 13. Nanoindentation test results of the coating:
(a) Load-displacement curves; (b) Hardness and elastic modulus; (c) H/E ; (d) H^3/E^2 .

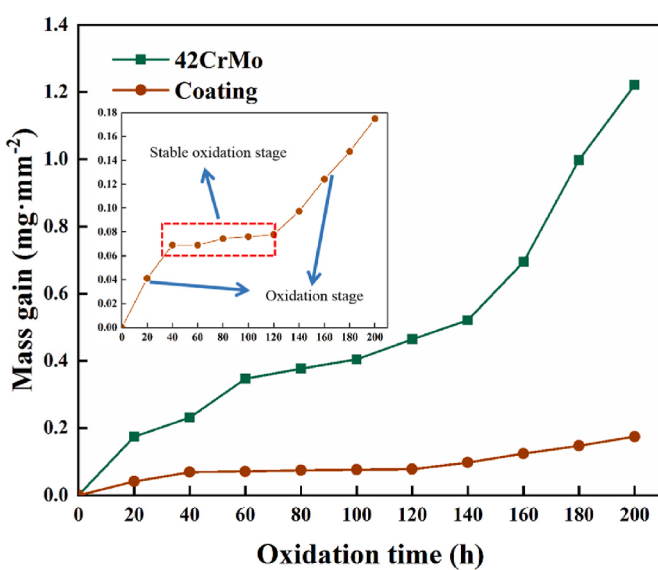


Fig. 14. Oxidation kinetics curves of 42CrMo steel and coating.

42CrMo steel was a complex wear mechanism of oxidative wear, abrasive wear, and adhesive wear [46]. The wear situation was reduced after elevated temperature oxidation due to the formation of a brittle oxide film with a higher microhardness on the surface of 42CrMo steel, and the wear mechanism was no significant difference.

3.2.3. Wear track profile and three-dimensional morphology

The wear track profile and morphology of the specimens before and after elevated temperature oxidation at room temperature are shown in Fig. 18. It was found that the microhardness correlated to the wear depth and width. The depth and width of the wear track profile of 42CrMo steel were deeper and larger and severe plastic deformation had occurred on both sides of the wear marks. The width and depth of the wear track profile of 42CrMo steel decreased after elevated temperature oxidation due to the increase of microhardness. The depth and width of the wear track profile of the coating were increase and slight plastic deformation occurred on both sides of the wear scar due to the reduction of microhardness.

3.2.4. Wear rate

The wear rate of the specimens before and after elevated temperature oxidation at room temperature are shown in Fig. 19. The wear rate is calculated by the following formula:

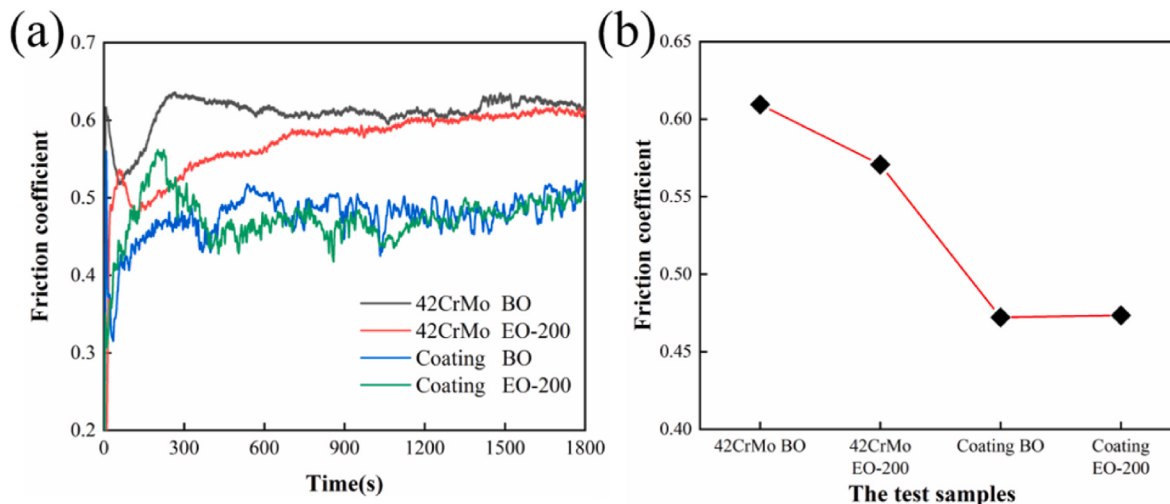
$$M = \frac{V}{L \cdot N} \quad (4)$$

where, M is the wear rate, V is the wear volume, L is the friction distance, and N is the normal load. As shown in the figure, the wear rate of 42CrMo steel after elevated temperature oxidation decreased from 0.2072 to 0.1424 $\text{mm}^3/\text{N} \cdot \text{m}$ due to the increase in surface microhardness. For the coating, the wear rate of the coating after elevated temperature oxidation increased from 0.0157 to 0.0236 $\text{mm}^3/\text{N} \cdot \text{m}$ due to the increase wear volume. The coating was shown to have excellent wear resistance due to the fact that the wear rate of the coating was considerably less than that of 42CrMo steel. The results showed that the wear rate was negatively correlated with the microhardness. It meant that the higher microhardness of the specimen, the stronger the

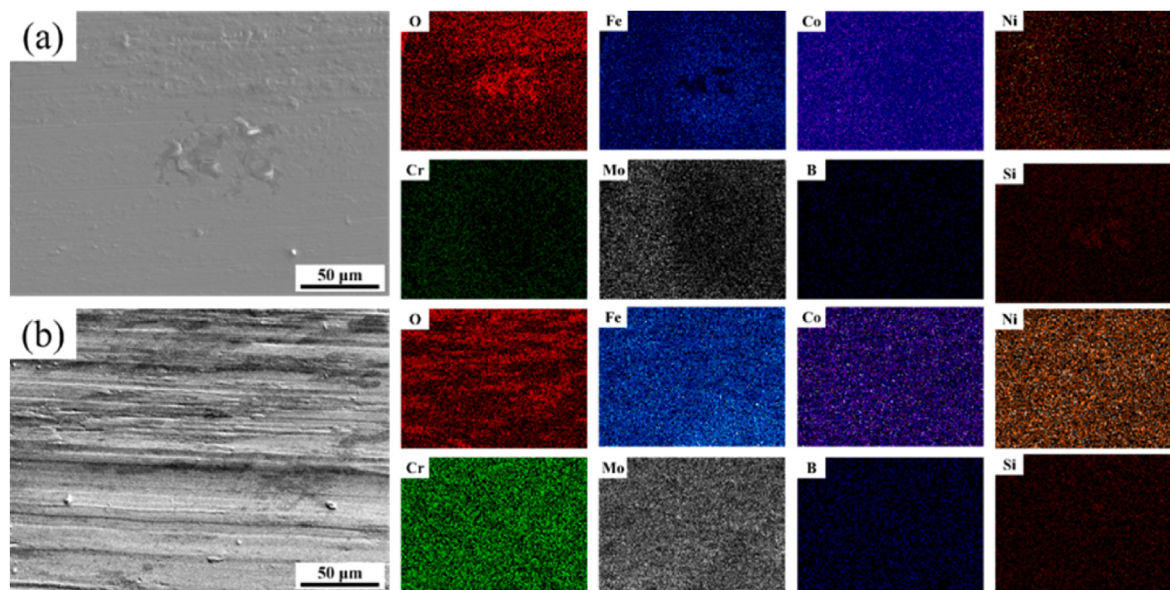
Table 5

Oxidation rate of 42CrMo steel and coating at each stage.

Oxidation stage (h)	Oxidation rate of 42CrMo (mg·mm ⁻² ·h ⁻¹)	Oxidation rate of coating (mg·mm ⁻² ·h ⁻¹)	Oxidation stage (h)	Oxidation rate of 42CrMo (mg·mm ⁻² ·h ⁻¹)	Oxidation rate of coating (mg·mm ⁻² ·h ⁻¹)
0–20	8.7×10^{-3}	2.05×10^{-3}	120–140	2.85×10^{-3}	0.98×10^{-3}
20–40	2.85×10^{-3}	1.4×10^{-3}	140–160	8.65×10^{-3}	1.34×10^{-3}
40–60	5.8×10^{-3}	0.1×10^{-3}	160–180	15.2×10^{-3}	1.16×10^{-3}
60–80	1.5×10^{-3}	0.17×10^{-3}	180–200	11.1×10^{-3}	1.16×10^{-3}
80–100	1.4×10^{-3}	0.08×10^{-3}	0–200	6.1×10^{-3}	0.87×10^{-3}
100–120	2.95×10^{-3}	0.09×10^{-3}			

**Fig. 15.** COF of 42CrMo steel and coating at room temperature:

(a) COF curve; (b) Average COF.

**Fig. 16.** Wear morphology and EDS of the coating at room temperature:

(a) Before oxidation; (b) After oxidation.

deformation resistance of the specimen, the lower the corresponding wear rate, and the better the wear resistance of the specimen.

3.3. Elevated temperature tribological performance

3.3.1. Coefficient of friction

The COF curves and the average COF of the specimens before and after elevated temperature oxidation at elevated temperature are shown in Fig. 20. A thicker oxide layer was generated on the surface of 42CrMo

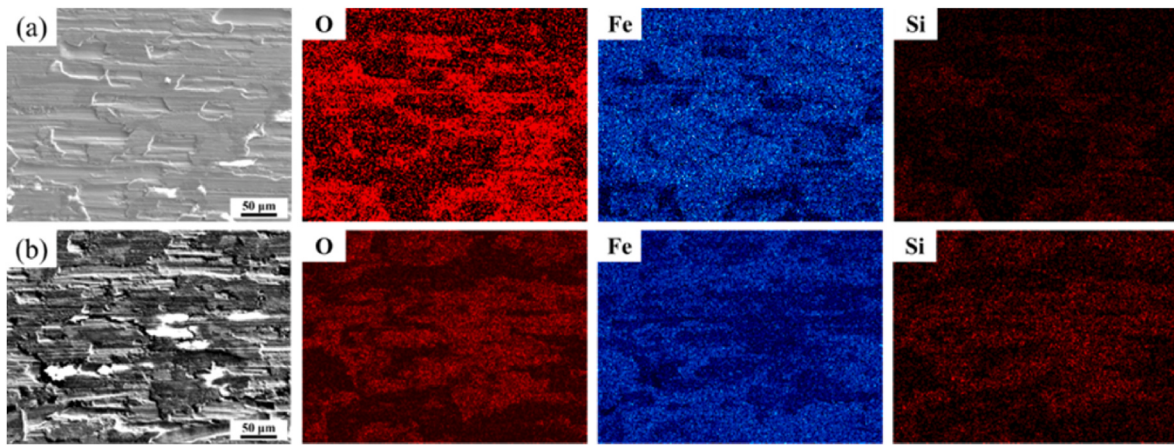


Fig. 17. Wear morphology and EDS of 42CrMo steel at room temperature:
(a) Before oxidation; (b) After oxidation.

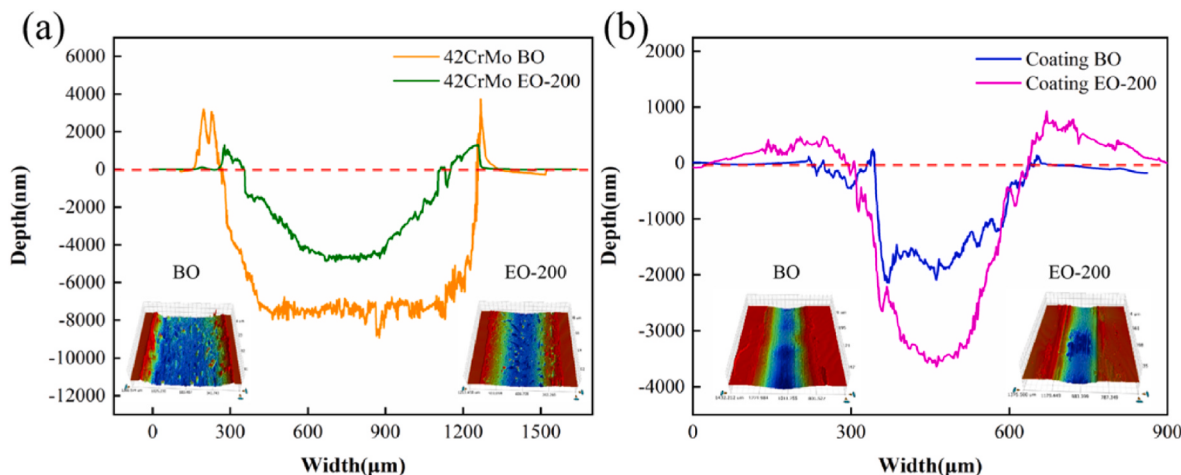


Fig. 18. Wear track profile and morphology of 42CrMo steel and coating at room temperature:
(a) 42CrMo; (b) Coating.

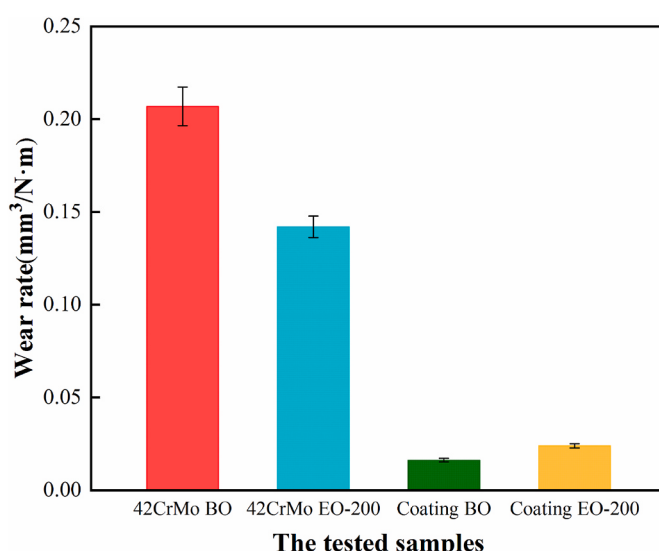


Fig. 19. Wear rate of 42CrMo steel and coating at room temperature.

steel after elevated temperature oxidation due to the poor oxidation resistance, which served as a lubricant and led to a lower COF in the early stages of wear. As the wear experiment progressed, the oxide film on the surface was destroyed and the COF gradually increased. However, the COF was low and the COF was also unstable at the later stage of wear due to the repeated formation of oxide film on 42CrMo steel surface in elevated temperature wear experiments. For the coating, the average COF before and after elevated temperature oxidation was not significantly discrepant due to the excellent elevated temperature oxidation resistance and abrasion resistance of the oxide film formed on the surface of the coating after elevated temperature oxidation.

As shown in Fig. 20(b), the average COF of the coating and 42CrMo steel after elevated temperature oxidation decreased from 0.461 to 0.406 and from 0.369 to 0.27, respectively. Comparing Figs. 15 and 20, the average COF of the coating at elevated temperature was not significant difference due to the excellent oxidation resistance and elevated temperature wear resistance of the dense oxide film formed on the surface of the coating. The average COF of 42CrMo steel at elevated temperature was about half that at room temperature due to the repeated formation of an oxide film with a lubricating properties on the surface of 42CrMo steel at elevated temperature.

3.3.2. Wear morphology

To investigate the effect of oxidation on the wear behavior of the

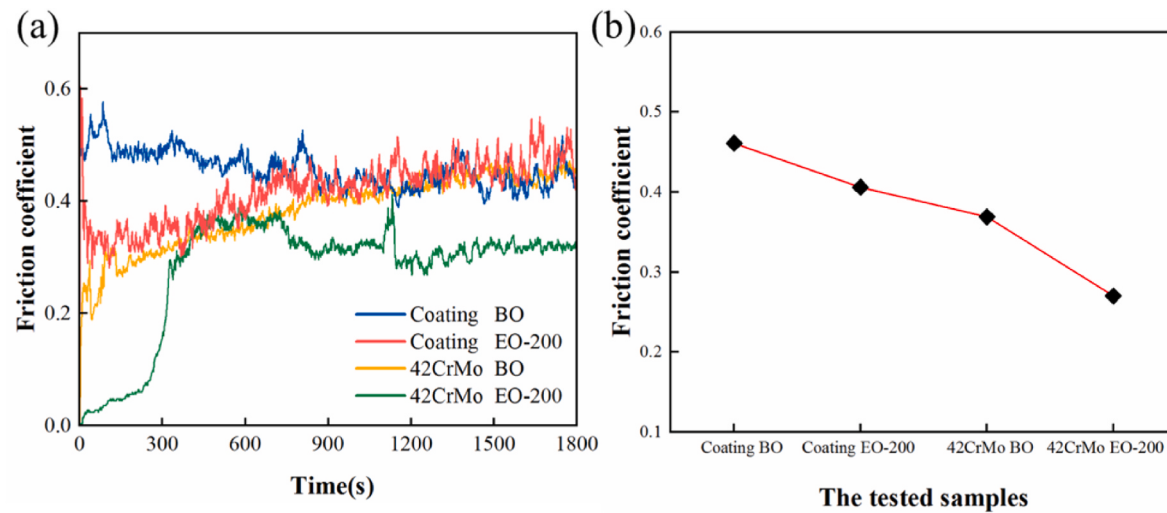


Fig. 20. COF of 42CrMo steel and coating at elevated temperature:
(a) COF curve (b) Average COF.

specimens at elevated temperature, SEM analysis is conducted on the wear surface, and the results are shown in Figs. 21 and 22. It could be seen that the wear surface of the coating before oxidation was relatively flat with shallow wear marks and O elements distribution on the wear surface was uniform, with only slight abrasive wear and oxidative wear occurring. The abrasive wear and oxidative wear aggravated after elevated temperature oxidation due to the reduction of microhardness and partial detachment of the oxide film on the wear surface. Compared with 42CrMo steel, the coating had excellent wear resistance at elevated temperature due to the dense and compact oxide film produced. The wear track on 42CrMo steel before and after oxidation were wide and deep due to the low microhardness, resulting in severe abrasive wear. In addition, severe oxidative wear occurred due to the alternating formation and stripping of the oxide film during the wear process. The wear of 42CrMo steel after elevated temperature oxidation was lower compared to that before oxidation due to the generation of a brittle oxide film that resisted a portion of the wear in the early stages of wear. In addition, the wear resistance of 42CrMo steel after elevated temperature oxidation

was improved due to the increase in surface microhardness.

3.3.3. Wear track profile and three-dimensional morphology

The wear track profile and morphology of the specimens before and after elevated temperature oxidation at elevated temperature are shown in Fig. 23. It could be seen that, the generated oxide layer fell off under the action of the friction ball due to the low microhardness of 42CrMo steel, resulting in severe plastic deformation and debris accumulation on both sides of the wear profile and the width and depth of the wear profile were relatively large. Compared with room temperature, the depth and width of the wear track profile of 42CrMo steel increased significantly at elevated temperature due to the repeated generation and peeling off of the oxide film. However, the depth and width of the wear track profile of the coating at room temperature and elevated temperature were not significant difference owing to the excellent elevated temperature wear resistance of the oxide film generated on the surface of the coating.

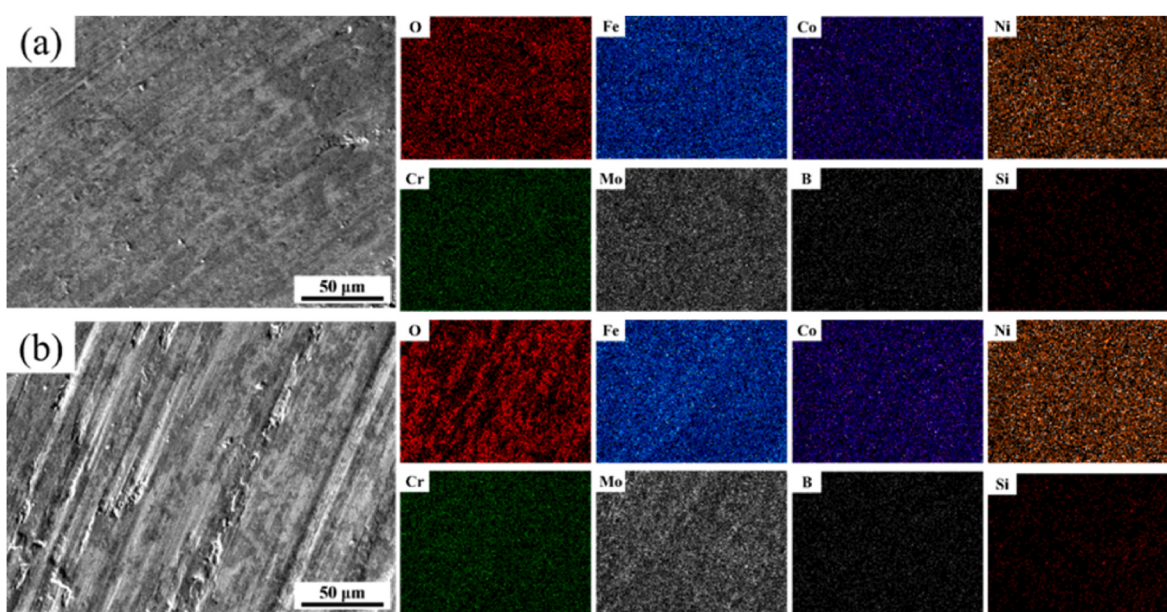


Fig. 21. Wear morphology and EDS of the coating at elevated temperature:
(a) Before oxidation; (b) After oxidation.

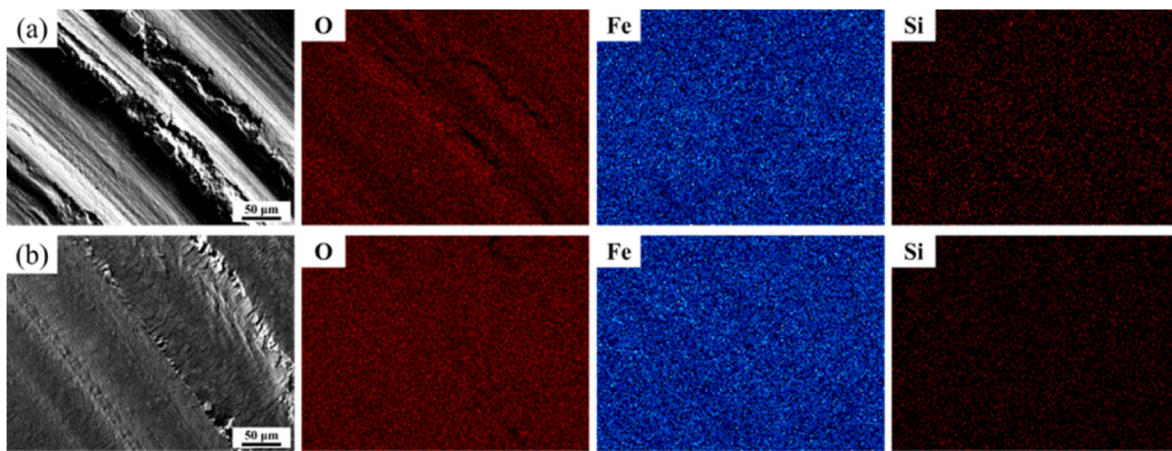


Fig. 22. Wear morphology and EDS of 42CrMo steel at elevated temperature: (a) Before oxidation; (b) After oxidation.

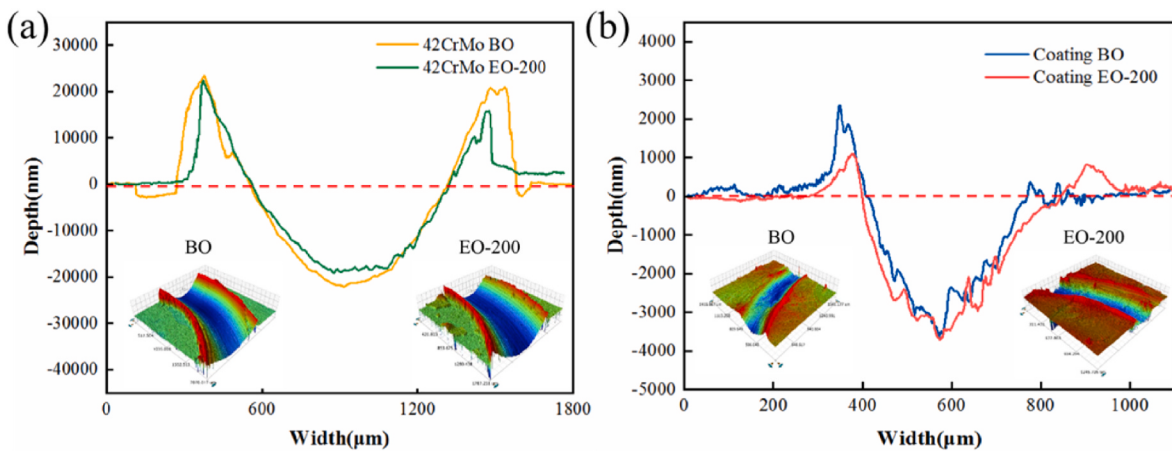


Fig. 23. Wear track profile and morphology of 42CrMo steel and coating at elevated temperature: (a) 42CrMo; (b) Coating.

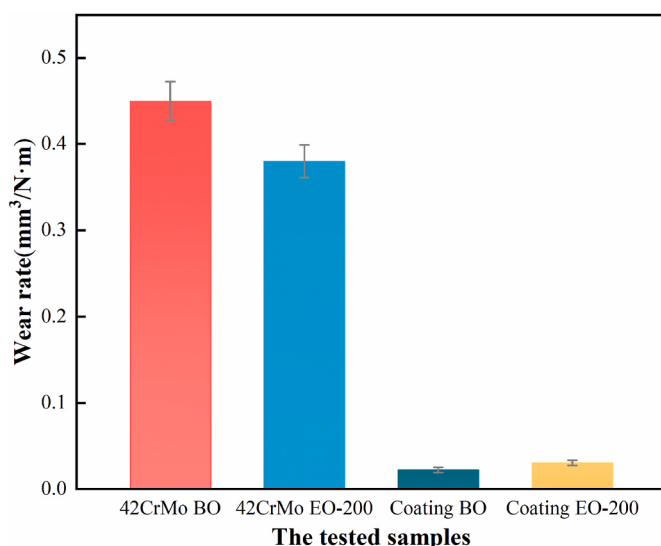


Fig. 24. Wear rate of 42CrMo steel and coating at elevated temperature.

3.3.4. Wear rate

The wear rate of the specimens before and after elevated temperature oxidation at elevated temperature are shown in Fig. 24. As shown in the

figure, the wear rate of 42CrMo steel decreased from $0.4512 \text{ mm}^3/\text{N}\cdot\text{m}$ to $0.3831 \text{ mm}^3/\text{N}\cdot\text{m}$, and the wear rate of the coating increased from $0.0224 \text{ mm}^3/\text{N}\cdot\text{m}$ to $0.0305 \text{ mm}^3/\text{N}\cdot\text{m}$. Compared with room temperature, the wear rate of 42CrMo steel was higher due to the repeated generation and peeling of oxides on 42CrMo surface at elevated temperature. On the contrary, the wear rate of the coating at room temperature and elevated temperature was not significant difference, indicating that the oxide film generated on the surface of the coating had excellent oxidation resistance and wear resistance at elevated temperature.

At present, most of the composite coatings and high-entropy alloy coatings prepared by researchers increased the wear resistance of 42CrMo steel by about 3 to 5 times[47, 48], while the Fe₂₀Co₂₀Ni₂₀Cr₈Mo₁₂B₁₀Si₁₀ high-entropy alloy coating prepared in this study not only increased the wear resistance of 42CrMo steel by about 10 times, but also had excellent elevated temperature properties. Therefore, the study was significant in improving the surface properties and service life of brake disc materials for high-speed trains.

4. Conclusion

Elevated temperature oxidation resistance and wear resistance of the Fe₂₀Co₂₀Ni₂₀Cr₈Mo₁₂B₁₀Si₁₀ high-entropy alloy coating were investigated. The following conclusions can be drawn:

- (1) The crystal structure of the coating changed from a dual-phase structure consisting of BCC (dominant phase) and FCC phase to a single FCC structure after 600 °C oxidation. And oxidation products SiO₂, MoO₃, Cr₂O₃ and NiCr₂O₄ appeared on the surface.
- (2) The isothermal oxidation test suggested that the coating possessed better oxidation resistance than 42CrMo steel with lower oxidation rate (about one fifth that of 42CrMo steel). The microhardness of the coating decreased after elevated temperature oxidation for 200 h due to the transformation from BCC phase to FCC phase.
- (3) The COF and the wear rate of the coating show no significant changes after elevated temperature oxidation 200 h. The wear mechanisms of the coating were mainly abrasive wear and oxidative wear. The wear resistance at elevated temperature decreased slightly compared to room temperature.
- (4) The wear resistance of the Fe₂₀Co₂₀Ni₂₀Cr₈Mo₁₂B₁₀Si₁₀ HEA coating was improved about 10 times and 20 times than that of 42CrMo steel at room temperature and elevated temperature.

Credit authors statement

Guosong Zhang: Conceptualization, Methodology, Writing-review & editing, Supervision, Funding acquisition. Zongjia Zhang, Di Jiang: Data curation, Resources, Writing-original draft, Investigation. Bing Chen, Jiyuan Xuan: Data curation and Investigation. Xiaojie Song: Formal analysis, Supervision, Funding acquisition.

Statement of Originality

As the corresponding author, I, Guosong Zhang, hereby confirm on behalf of all authors that:

- 1) The paper has not been published previously, that it is not under consideration for publication elsewhere, and that if accepted it will not be published elsewhere in the same form, in English or in any other language, without the written consent of the publisher.
- 2) The paper does not contain material which has been published previously, by the current authors or by others, of which the source is not explicitly cited in the paper.

Declaration of competing interest

The authors declare that they have no known competing financial interests or personal relationships that could have appeared to influence the work reported in this paper.

Acknowledgements

This project is supported by National Natural Science Foundation of China (Grant No.U2106126, and 52331004), Qingdao Natural Science Foundation (Grant No.23-2-1-213-zyyd-jch, and 23-2-1-93-zyyd-jch).

References

- [1] Sun D, Cai YC, Zhu LS, Gao FF, Shan MD, Manladan SM, et al. High-temperature oxidation and wear properties of TiC-reinforced CrMnFeCoNi high entropy alloy composite coatings produced by laser cladding. Surf Coating Technol 2022;438: 128407. <https://doi.org/10.1016/j.surcoat.2022.128407>.
- [2] Xie FW, He YH, Yuan ZR, Kang XY. Microstructure and high-temperature sliding wear performance of Fe-Co-Mo alloy coating fabricated by plasma cladding. Surf Coating Technol 2022;444:128667. <https://doi.org/10.1016/j.surcoat.2022.128667>.
- [3] Zhang SY, Han B, Li MY, Zhang Q, Hu CY, Jia CX, et al. Microstructure and high temperature erosion behavior of laser cladded CoCrFeNiSi high entropy alloy coating. Surf Coating Technol 2021;417:127218. <https://doi.org/10.1016/j.surcoat.2021.127218>.
- [4] Shi FK, Zhang QK, Xu C, Hu FQ, Yang LJ, Zheng BZ, et al. In-situ synthesis of NiCoCrMnFe high entropy alloy coating by laser cladding. Opt Laser Technol 2022; 151:108020. <https://doi.org/10.1016/j.optlastec.2022.108020>.
- [5] Hong S, Shi XL, Lin JR, Wu YP, Li JH, Zheng Y. Microstructure and cavitation-silt erosion behavior of two HVOF-sprayed hardfacing coatings for hydro-turbine applications. Alex Eng J 2023;69:483–96. <https://doi.org/10.1016/j.aej.2023.02.010>.
- [6] Hong S, Wei ZY, Lin JR, Sun W, Zheng Y. Cavitation-silt erosion behavior and mechanism in simulated sea water slurries of cermet coatings manufactured by HVOF spraying. Ceram Int 2023;49:14355–66. <https://doi.org/10.1016/j.ceramint.2023.01.024>.
- [7] Cheng JB, Liang XB, Xu BS. Devitrification of arc-sprayed FeBSiNb amorphous coatings: effects on wear resistance and mechanical behavior. Surf Coating Technol 2013;235:720–6. <https://doi.org/10.1016/j.surfcoat.2013.08.054>.
- [8] Shen QK, Xue JX, Yu XY, Zheng ZH, Ou N. Triple-wire plasma arc cladding of Cr-Fe-Ni-Ti_x high-entropy alloy coatings. Surf Coating Technol 2022;443:128638. <https://doi.org/10.1016/j.surfcoat.2022.128638>.
- [9] Liang DD, Zhou YH, Liu XD, Zhou Q, Huang B, Zhang EG, et al. Wettability and corrosion performance of arc-sprayed Fe-based amorphous coatings. Surf Coating Technol 2022;443:128129. <https://doi.org/10.1016/j.surfcoat.2022.128129>.
- [10] Jiao XY, Wang CM, Gong ZQ, Wang GM, Sun HF, Yang HR. Effect of Ti on Ti5M composite coating fabricated by laser cladding technology. Surf Coating Technol 2017;325:643–9. <https://doi.org/10.1016/j.surfcoat.2017.07.008>.
- [11] Chang W, Xiao GC, Zhang H, Chen H, Yi MD, Zhang JJ, et al. Microstructure and properties of graphene reinforced co-based composite coating by laser cladding. Surf Coating Technol 2023;453:129139. <https://doi.org/10.1016/j.surfcoat.2022.129139>.
- [12] Wang JY, Cui XF, Jin G, Zhao Y, Wen X, Zhang Y. Effect of in-situ Ni interlayer on the microstructure and corrosion resistance of underwater wet 316L stainless steel laser cladding layer. Surf Coating Technol 2023;458:129341. <https://doi.org/10.1016/j.surfcoat.2023.129341>.
- [13] Nayak MK, Roy S, Manna I. Effect of substrate surface roughness on the microstructure and properties of laser surface cladding of Tribaloy T-400 on mild steel. Surf Coating Technol 2023;455:129210. <https://doi.org/10.1016/j.surfcoat.2022.129210>.
- [14] Nie BX, Xue YP, Wang XM, Ding YH, Fu K, Zhong C, et al. On the elemental segregation and melt flow behavior of pure copper laser cladding. Surf Coating Technol 2023;452:129085. <https://doi.org/10.1016/j.surfcoat.2022.129085>.
- [15] Jiang D, Li Z, Xu JJ, Ren QY, Agbedor SO, Lei Q. High-temperature oxidation behaviors of an equiatomic CrMnFeCoNi high entropy alloy. Mater Today Commun 2022;32:104185. <https://doi.org/10.1016/j.mtcomm.2022.104185>.
- [16] He LX, Liu CH, Zhao S, Shu CZ, Yang JJ, Liu HQ, et al. Microstructure, mechanical and corrosion properties of high hardness TiVzrCrAl HEA coatings prepared by magnetron sputtering. Surf Coating Technol 2022;441:128532. <https://doi.org/10.1016/j.surfcoat.2023.128532>.
- [17] He R, Wu MP, Cui C, Jie DD, Gong YL, Miao XJ. Microstructure evolution, mechanical properties of FeCrNiMnAl high entropy alloy coatings fabricated by laser cladding. Surf Coating Technol 2022;447:128851. <https://doi.org/10.1016/j.surfcoat.2022.128851>.
- [18] Zhang MN, Wang DF, He LJ, Ye XY, Ouyang WT, Xu ZF, et al. Microstructure and elevated temperature wear behavior of laser-cladded AlCrFeMnNi high-entropy alloy coating. Opt Laser Technol 2022;149:107845. <https://doi.org/10.1016/j.optlastec.2022.107845>.
- [19] Sun ZP, Zhang XY, Li XZ, Xu ZM, Li C, Wang ZM. Study on the wear behavior of CoCrFeNiAl_{1.0} high entropy alloy at high temperature. Mater Lett 2022;324: 132726. <https://doi.org/10.1016/j.matlet.2022.132726>.
- [20] Zhuang DD, Tao WW, Ni HM, Wang AZ, Du B, Zhang SH, et al. TiC distribution and properties of TiC-CrMnFeCoNi coating fabricated by laser cladding with ultrasound. Surf Coating Technol 2023;468:129744. <https://doi.org/10.1016/j.surfcoat.2023.129744>.
- [21] Ge YY, Cheng JB, Mo JY, Xue L, Zhang BS, Hong S, Wu YP, Liang XB, Zhang XC. Experimental and DFT studies on corrosion behaviors of laser-cladded (FeCoNi)_{75-x}Cr_xB₁₅Si₁₀ high-entropy alloy coatings. J Alloys Compd 2024;976: 173173. <https://doi.org/10.1016/j.jallcom.2023.173173>.
- [22] Ma ZS, Xia CQ, Zhong H, Yang T, Liu N, Liang CY, et al. Microstructure, mechanical property and corrosion resistance of FeCoCrNi-M high-entropy alloy coatings on 6061 aluminum alloy prepared by laser cladding. Surf Coating Technol 2023;455: 129217. <https://doi.org/10.1016/j.surfcoat.2022.129217>.
- [23] Guan YJ, Cui XF, Chen D, Su WN, Zhao Y, Li J, et al. Realizing high strength and toughness of gradient high-entropy alloy coating by in-situ interface reaction of FeCoCrNi/FeCoCrAl. Surf Coating Technol 2023;464:129569. <https://doi.org/10.1016/j.surfcoat.2023.129569>.
- [24] Peng YB, Zhang W, Li TC, Zhang MY, Liu B, Liu Y, et al. Effect of WC content on microstructures and mechanical properties of FeCoCrNi high-entropy alloy/WC composite coatings by plasma cladding. Surf Coating Technol 2020;385:125326. <https://doi.org/10.1016/j.surfcoat.2019.125326>.
- [25] Xu Z, Li QY, Li W, Li DY. Microstructure, mechanical properties, and wear behavior of AlCoCrFeNi high-entropy alloy and AlCrFeNi medium-entropy alloy with WC addition. Wear 2023;522:204701. <https://doi.org/10.1016/j.wear.2023.204701>.
- [26] Deng C, Wang C, Chai LJ, Wang T, Luo J. Mechanical and chemical properties of CoCrFeNiMo_{0.2} high entropy alloy coating fabricated on Ti6Al4V by laser cladding. Intermetallics 2022;144:107504. <https://doi.org/10.1016/j.intermet.2022.107504>.
- [27] Li YF, Zhang J, Huang XH, Liu J, Deng LJ, Han PY. Influence of laser power on microstructure evolution and properties of laser cladded FeNiCoCrMo HEA

- coatings. *Mater Today Commun* 2023;35:105615. <https://doi.org/10.1016/j.mtcomm.2023.105615>.
- [28] Wang Z, Zhu J, Guo YM, Xin WH, Hui XD, Wu YL, Zheng HY, Zhao Y, Wang XM. Multi-effects of Mo on enhancement of wear and corrosion resistances of FeCoNiCrMo high entropy alloys coatings prepared by laser powder directed energy deposition. *Surf Coating Technol* 2024;477:130378. <https://doi.org/10.1016/j.surfcoat.2024.130378>.
- [29] Zhang C, Chen GJ, Dai PQ. Evolution of the microstructure and properties of laser-clad FeCrNiCoB_x high-entropy alloy coatings. *Mater Sci Technol* 2016;32(16): 1666–72. <https://doi.org/10.1080/02670836.2015.1138035>.
- [30] Yang YC, Ren YJ, Tian YW, Li KY, Bai LC, Huang QL, et al. Microstructure and tribological behaviors of FeCoCrNiMoSi_x high-entropy alloy coatings prepared by laser cladding. *Surf Coating Technol* 2022;432:128009. <https://doi.org/10.1016/j.surfcoat.2021.128009>.
- [31] Liu YY, Yao ZP, Zhang P, Xu Z, Lin SY, He MY, et al. Tailoring high-temperature oxidation resistance of FeCrMnVSi high entropy alloy coatings via building Si-rich dendrite microstructure. *Appl Surf Sci* 2022;606:154862. <https://doi.org/10.1016/j.apsusc.2022.154862>.
- [32] Jia L, Jiang LW, Zheng WL, Wu JW, Feng JL. Function of Si on the high-temperature oxidation of FeCoNiMnSi_x HEAs with excellent electromagnetic-wave absorption properties. *J Alloys Compd* 2023;950:169853. <https://doi.org/10.1016/j.jallcom.2023.169853>.
- [33] Yu Q, Wang CS, Yang G, Ren YH, Liu NX, Liang YP, Dong C. Influence of Cr/Mo ratio on microstructure and mechanical properties of the Ni-based superalloys fabricated by laser additive manufacturing. *J Alloys Compd* 2022;894:162484. <https://doi.org/10.1016/j.surfcoat.2021.162484>.
- [34] Zhang GS, Liu T, Yin QH, Wang WC, Song XJ, Huang WM, et al. Effect of B-Si ratio and laser remelting on the microstructure and properties of Fe₁₀Co₁₀Ni₁₀Cr₄Mo₆B₈Si_{10-x} coating by laser cladding. *Surf Coating Technol* 2022; 450:128989. <https://doi.org/10.1016/j.surfcoat.2022.128989>.
- [35] Chen B, Zhang GS, Zhang ZJ, Wang ZY, Guo CF, Song XJ. Improved wear and corrosion resistance of laser-clad (Fe_{0.25}Co_{0.25}Ni_{0.25}Cr_{0.125}Mo_{0.125})₈₆B₁₄ coating through annealing treatment. *Surf Coating Technol* 2023;473:129973. <https://doi.org/10.1016/j.surfcoat.2023.129973>.
- [36] Löbel M, Lindner T, Lampke T. High-temperature wear behaviour of AlCoCrFeNiTi_{0.5} coatings produced by HVOF. *Surf Coating Technol* 2020;403: 126379. <https://doi.org/10.1016/j.surfcoat.2020.126379>.
- [37] Lin YT, Li JF, Chen SY, Zhou HD, Shu YM, Tang LQ, et al. In situ construction of pyrite-marcasite-magnetite composite via FeS₂ phase transformation and oxidation for the synergistic degradation of methyl orange and Cr(VI). *Separ Purif Technol* 2023;308:122764. <https://doi.org/10.1016/j.surfcoat.2022.122764>.
- [38] Li NH, Chen YH, Hu CY, Hsieh CH, Lo SL. Stabilization of nickel-laden sludge by a high-temperature NiCr₂O₄ synthesis process. *J Hazard Mater* 2011;198:356–61. <https://doi.org/10.1016/j.jhazmat.2011.10.077>.
- [39] Babicheva R, Jarlöv A, Zheng H, Dmitriev S, Korznikova E, Ling Sharon Nai M, et al. Effect of short-range ordering and grain boundary segregation on shear deformation of CoCrFeNi high-entropy alloys with Al addition. *Comput Mater Sci* 2022;215:111762. <https://doi.org/10.1016/j.commatsci.2022.111762>.
- [40] Gorr B, Mueller F, Christ HJ, Mueller T, Chen H, Kauffmann A, et al. High temperature oxidation behavior of an equimolar refractory metal-based alloy 20Nb-20Mo-20Cr-20Ti-20Al with and without Si addition. *J Alloys Compd* 2016; 688:468–77. <https://doi.org/10.1016/j.jallcom.2016.07.219>.
- [41] Liang ZD, Göken M, Lorenz U, Neumeier S, Oehring M, Pyczak F, et al. Influence of small amounts of Si and Cr on the high temperature oxidation behavior of novel cobalt base superalloys. *Corrosion Sci* 2021;184:109388. <https://doi.org/10.1016/j.corsci.2021.109388>.
- [42] Zeng X, Liu ZY, Wu GG, Tong X, Xiong YQ, Cheng XD, et al. Microstructure and high-temperature properties of laser cladded AlCoCrFeNiTi_{0.5} high-entropy coating on Ti-6Al-4V alloy. *Surf Coating Technol* 2021;418:127243. <https://doi.org/10.1016/j.surfcoat.2021.127243>.
- [43] Xiao Q, Li SY, Yang WB, Yang CH, Chen DY, Ding HH, et al. High-temperature tribological properties of coatings repaired by laser additive manufacturing on railway wheel tread damage. *Wear* 2023;520–521:204674. <https://doi.org/10.1016/j.wear.2023.204674>.
- [44] Zhu ZX, Liu XB, Liu YF, Zhang SY, Meng Y, Zhou HB, et al. Effects of Cu/Si on the microstructure and tribological properties of FeCoCrNi high entropy alloy coating by laser cladding. *Wear* 2023;512–513:204533. <https://doi.org/10.1016/j.wear.2022.204533>.
- [45] Rymer LM, Lindner T, Lampke T. Enhanced high-temperature wear behavior of high-speed laser metal deposited Al_{0.3}CrFeCoNi coatings alloyed with Nb and Mo. *Surf Coating Technol* 2023;470:129832. <https://doi.org/10.1016/j.surfcoat.2023.129832>.
- [46] Xie FW, He YH, Yuan ZR, Kang XY. Microstructure and high-temperature sliding wear performance of Fe-Co-Mo alloy coating fabricated by plasma cladding. *Surf Coating Technol* 2022;444:128667. <https://doi.org/10.1016/j.surfcoat.2022.128667>.
- [47] Lv GJ, Yang XF, Gao YL, Wang SR, Xiao JP, Zhang YF, Chen KY, Yang H. Investigation on fretting Wear performance of laser cladding WC/Co₆ coating on 42CrMo steel for hydraulic damper. *Int J Refract Metals Hard Mater* 2023;111: 106068. <https://doi.org/10.1016/j.ijrmhm.2022.106068>.
- [48] Wan L, Cheng MY, Fu GY, Wei C, Shi T, Shi SH. Annular laser cladding of CuPb10Sn10 copper alloy for high-quality anti-friction coating on 42CrMo steel surface. *Opt Laser Technol* 2023;158:108878. <https://doi.org/10.1016/j.optlastec.2022.108878>.